INL/RPT-24-77296

Characterization of Intrinsic Fiber Optic Temperature Sensors by In-core and Furnace Testing

March 2024

Kelly McCary

Austin Fleming

INL/RPT-24-77296

Characterization of Intrinsic Fiber Optic Temperature Sensors by In-core and Furnace Testing

Kelly McCary
Austin Fleming

March 2024

Idaho National Laboratory
Idaho Falls, Idaho 83415

http://www.inl.gov

Prepared for the
U.S. Department of Energy
Office of Nuclear Energy
Under DOE Idaho Operations Office
Contract DE-AC07-05ID14517

Page intentionally left blank

CONTENTS

FIGURES

TABLES

ACRONYMS

ATR	Advanced Test Reactor
FBG	fiber Bragg grating
PSC	pure silica core
RIC	radiation-induced compaction

Page intentionally left blank

Characterization of Intrinsic Fiber Optic Temperature Sensors by In-core and Furnace Testing

1. INTRODUCTION

Increased nuclear technology R&D has raised the demand for novel sensors and instrumentation that can meet all data objectives and survive under various conditions and environments beyond conventional light-water reactor environments. Expediting the deployment of advanced nuclear technologies by developing, demonstrating, and qualifying advanced reactor fuel forms necessitates a deeper understanding of how irradiation affects fuel and material performance. To achieve a more comprehensive understanding of fuels and materials performance, researchers require more specialized experiments and measurements.

The demand for innovative sensors to support nuclear fuel development arises from the complexity of material behavior under irradiation and the challenges of deploying irradiation testing instrumentation in material test reactors. Additionally, material property measurements require integrated measurement systems in order to characterize thermal and mechanical properties, chemistry, and microstructure. [1] Among the potential measurement techniques, optical-fiber-based sensors have been identified as candidate sensors for measuring physical phenomena such as temperature, strain, pressure, and fluid level.

Optical fiber sensors can serve as multi-sensing and multiplexing instrumentation, enabling measurement of different physical parameters via a single sensor configuration, and transmitting—through a single fiber—data collected from multiple locations. They are cost-effective, immune to electromagnetic interference, electrically passive, and compatible with various sensing methodologies. Beyond their widespread use in telecommunications, silica-fiber-based instruments are also utilized in industrial applications (even at temperatures reaching 300°C–400°C) such as distributed temperature sensing in oil and gas recovery.

The U.S. Department of Energy is interested in using fiber optics to support fuel cycle development, [2] as fiber optics are an excellent candidate for harsh environment sensing, including sensing at very high temperatures (1900°C for sapphire optical fibers). Distributed fiber optic sensing has already been deployed in various harsh environments (e.g., coal gasification plants). [3] Distributed strain sensing, which operates similarly to distributed temperature sensing, has been deployed to monitor underground mines, and fibers have been imbedded in soil to monitor sink-hole development. [4-5] This all makes the application of fiber optic sensors to advanced reactor development a promising area of research.

2. HIGH-TEMPERATURE TESTING

One limitation of optical fiber sensors is high temperatures, which can cause optical frequency domain reflectometry sensing failure in optical fiber whenever defects anneal out with temperature and change the backscatter profile of the fiber or cause it to undergo mechanical failure. Mechanical failures in optical fiber can stem from failure of the coating on the fiber.

2.1 Experiment Methodology

Iterative referencing schemes have extended the operational range of silica optical fibers for short times up to 1000°C. At such high temperatures, most coating options for silica optical fiber will have burned off. The following are some recommended maximum operating temperatures for various coating types (i.e., the operating limits listed by the manufacturers):

- Polyimide (350°C) [6]
- Aluminum (400°C) [7]

- Copper (~600°C) [7]
- Gold (~700°C). [7]

To extend the operational temperature of coated silica fiber optic sensors, some metalized fibers were placed in a furnace and then tested in regard to their sensing capabilities. Two furnace tests were completed, covering four different coating types. The first test benchmarked aluminum (Al)- and copper-carbon (Cu-C)-coated optical fibers against a polyimide-coated optical fiber. The metal-coated fibers were purchased from IVG Fibers. For the first test, four optical fibers were placed in a tube furnace with a type-K thermocouple in air and then heated up to 700°C. Figure 1 shows the temperature profile used. The fibers were interrogated using a Luna Innovations Optical Backscatter Reflectometer, and the spectral shifts along their lengths were recorded at each temperature hold. The fibers were terminated with an angled cleave, and were connected to the Optical Backscatter Reflectometer via an FC/APC connector.

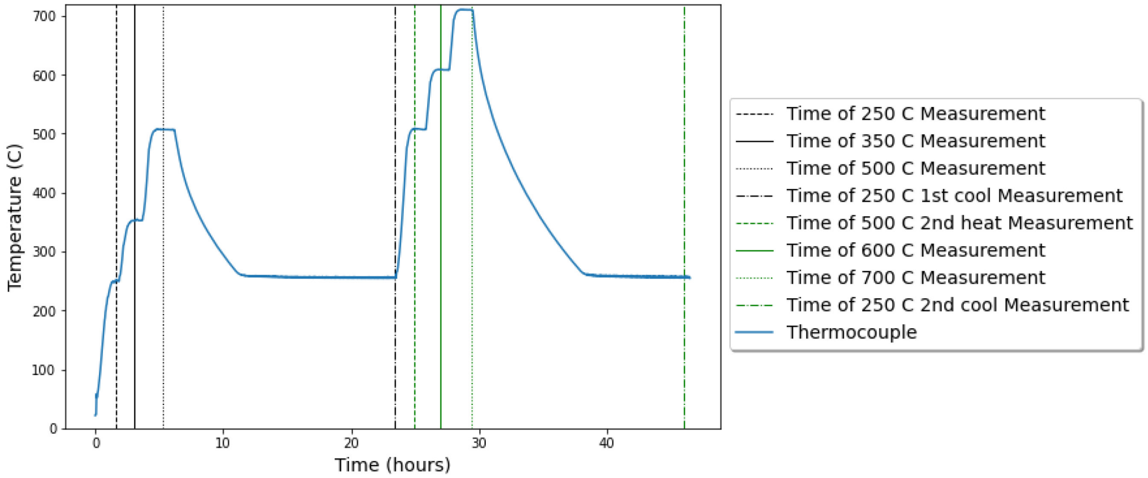

Figure 1. Temperature profile for the benchmark testing of metalized fibers, with the times of data collection for each temperature being indicated.

The second thermal test was conducted with gold (Au)- and Cu-C-coated optical fibers. The Cu-C fiber was also manufactured by IVG Fibers. The Au fiber was custom ordered from Fiber Guide Inc as a single-mode silica gold-coated fiber. The fibers were placed in a tube furnace that was configured to allow argon gas to flow through the heated region, thereby maintaining an inert environment. The fibers and a type-K thermocouple were heated via a series of thermal anneals and profiles with peak temperatures ranging from 500°C up to 700°C. Table 1 and Table 2 list the temperature-time profiles used for the thermal cycling, and Table 3 lists the order of the temperature-time profiles. These temperature-time profiles were chosen in order to test the repeatability of the spectral shift in the fibers over a range of temperatures during both sensor heating and cooling. The fibers were interrogated using an ODiSI, and were terminated with termination fiber to reduce the noise stemming from the end reflection. To pass the fibers into the inert gas environment, they were epoxied into a stainless-steel capillary tube near the connectors. The tubes were then placed through vacuum feedthroughs with rubber gasket compression seals.

Table 1. Temperature-time profiles 1 and 2 for the cyclical thermal testing of metal-coated silica optical fibers.

Profile 1			Profile 2		
Step	Type	Temperature (°C)	Step	Type	Temperature (°C)
1	ramp	250	1	ramp	250
2	hold	250	2	hold	250

Profile 1			Profile 2		
Step	Type	Temperature (°C)	Step	Type	Temperature (°C)
3	ramp	300	3	ramp	400
4	hold	300	4	hold	400
5	ramp	400	5	ramp	500
6	hold	400	6	hold	500
7	ramp	500	7	ramp	600
8	hold	500	8	hold	600
9	ramp down	400	9	ramp down	400
10	hold	400	10	hold	400
11	ramp down	300	11	ramp down	300
12	hold	300	12	hold	300
13	ramp	0	13	ramp	0
14	end	0	14	end	0

Table 2. Temperature-time profiles 3 and 4 for the cyclical thermal testing of metal-coated silica optical fibers.

Profile 3			Profile 4		
Step	Type	Temperature (°C)	Step	Type	Temperature (°C)
1	ramp	250	1	ramp	250
2	hold	250	2	hold	250
3	ramp	300	3	ramp	300
4	hold	300	4	hold	300
5	ramp	400	5	ramp	400
6	hold	400	6	hold	400
7	ramp	500	7	ramp	500
8	hold	500	8	hold	500
9	ramp	600	9	ramp	600
10	hold	600	10	hold	600
11	ramp down	500	11	ramp	700
12	hold	500	12	hold	700
13	ramp down	300	13	ramp down	500
14	hold	300	14	hold	500
15	ramp	0	15	ramp down	300
16	end	0	16	hold	300
			17	ramp	0
			18	end	0

Table 3. Cycle order for the thermal testing of metal-coated silica optical fibers.

Cycle	Profile
1	1
2	1
3	1
4	2
5	1
6	1
7	3
8	3
re-reference	
9	3
10	3
11	700°C Anneal
12	4
13	4

2.2 Experiment Results and Discussion

The four fibers in the first thermal test of the metal-coated silica fibers responded well. For the polyimide-coated silica fiber, Figure 2 and Figure 3 show the spectral shift at each of the temperature holds. The coating for the polyimide fiber would burn off at some point between the 350°C and 500°C temperature steps, leaving the sensors as nothing more than bare silica fiber. Polyimide fiber #2 showed good repeatability at 250°C and 500°C, whereas polyimide fiber #1 appears to have broken while cooling from 700°C back down to 250°C. This is expected, as the fibers were bare at that time. The Al-coated optical fiber responded well through the first thermal cycle, but failed at 700°C. The response of the Al-coated fiber is shown in Figure 4. Upon removal of the fibers, the Al-coated fiber's coating was seen to have melted and beaded up at one location on the fiber. The break in the fiber was located in the section where the Al coating had melted off. The Cu-C-coated fiber response is depicted in Figure 5. The Cu-C fiber responded well and showed good repeatability at 500°C, but poor repeatability at 250°C after the first heat to 500°C—and especially after being heated to 700°C. This is likely due to oxidation of the copper coating having caused stresses on the fiber, thus preventing it from relaxing back into its initial reference state. [8] This can be addressed by maintaining an inert environment or, prior to deployment, by heat treating the fiber beyond the maximum desired operation temperature. The noise at the fiber ends is caused by the end reflections of the optical fibers.

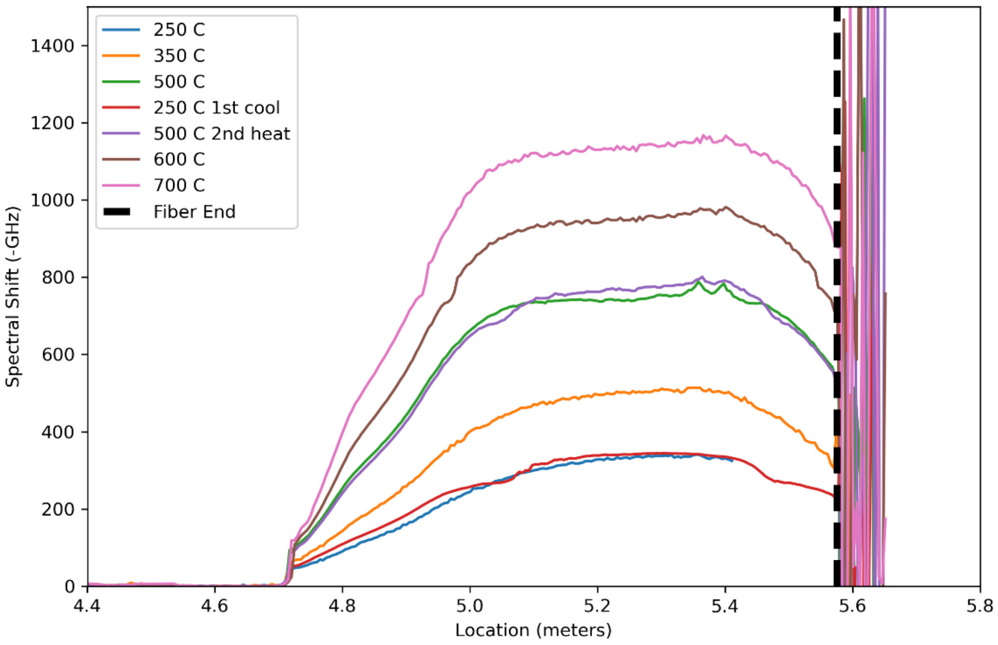

Figure 2. Spectral shift of polyimide-coated fiber #1 when heated to 700°C. This fiber failed when being cooled from 700°C to 250°C.

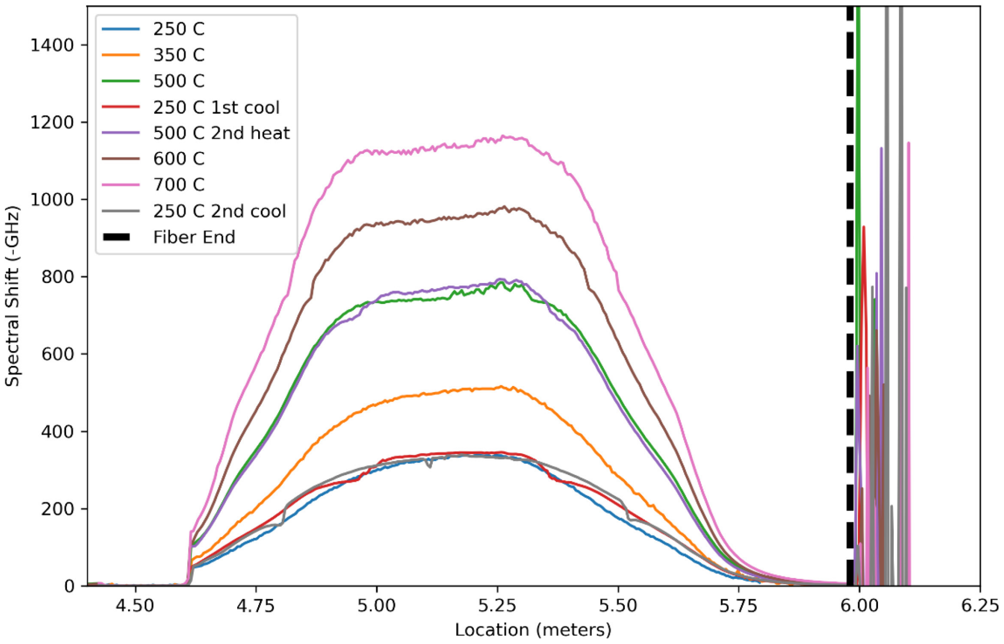

Figure 3. Spectral shift of polyimide-coated fiber #2 when heated to 700°C.

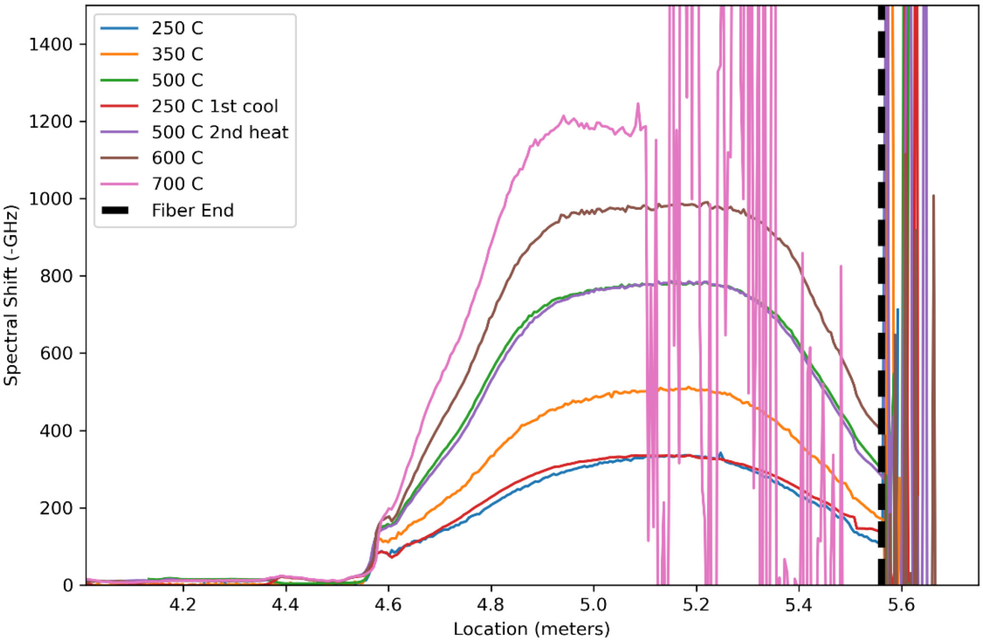

Figure 4. Spectral shift of Al-coated optical fiber when heated to 700°C.

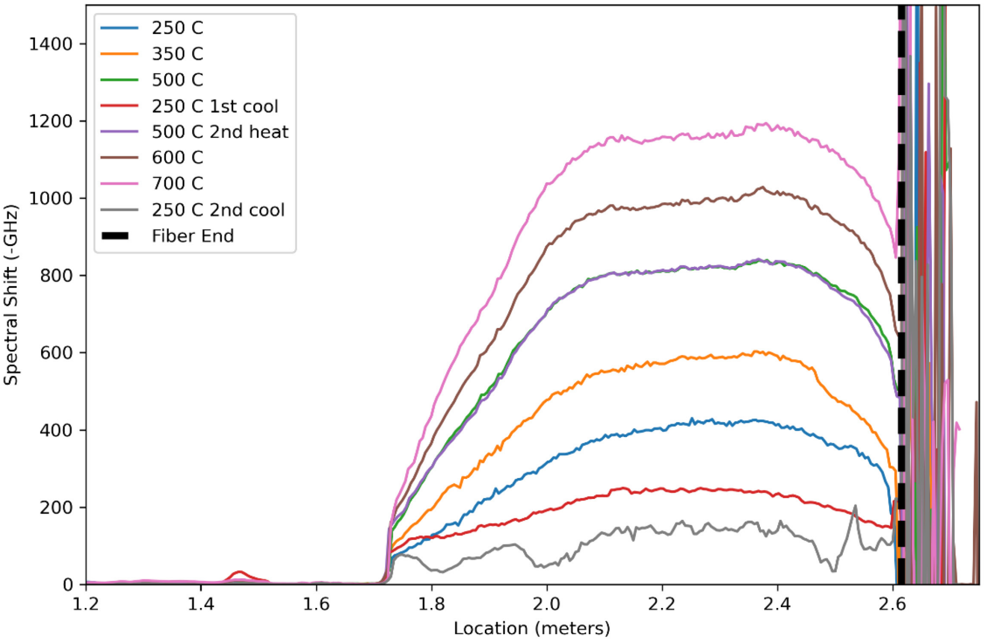

Figure 5. Spectral shift of Cu-C-coated fiber when heated to 700°C.

The second thermal test was designed for two main purposes: (1) to test the newly acquired Au-coated fiber and (2) to test the Cu-C-coated fiber in an inert environment to avoid any oxidation effects. These fibers were terminated with coreless termination fiber to reduce the noise at the end of the fiber, and they were interrogated using the ODiSI in order to allow for continuous interrogation over the entire thermal cycle. Unfortunately, the computer recording the thermocouple data for the test malfunctioned and corrupted the data files, so no thermocouple data are included in these results. Figure 6 and Figure 7 show, respectively, the response of the Au-coated and the Cu-C-coated optical fibers over all the thermal cycles. They also show the peak temperature of each cycle, along with where the reference scans for the sensors were updated. Both sensors survived the test and responded to temperature changes and holds (up to and including 700℃) without suffering coating failure.

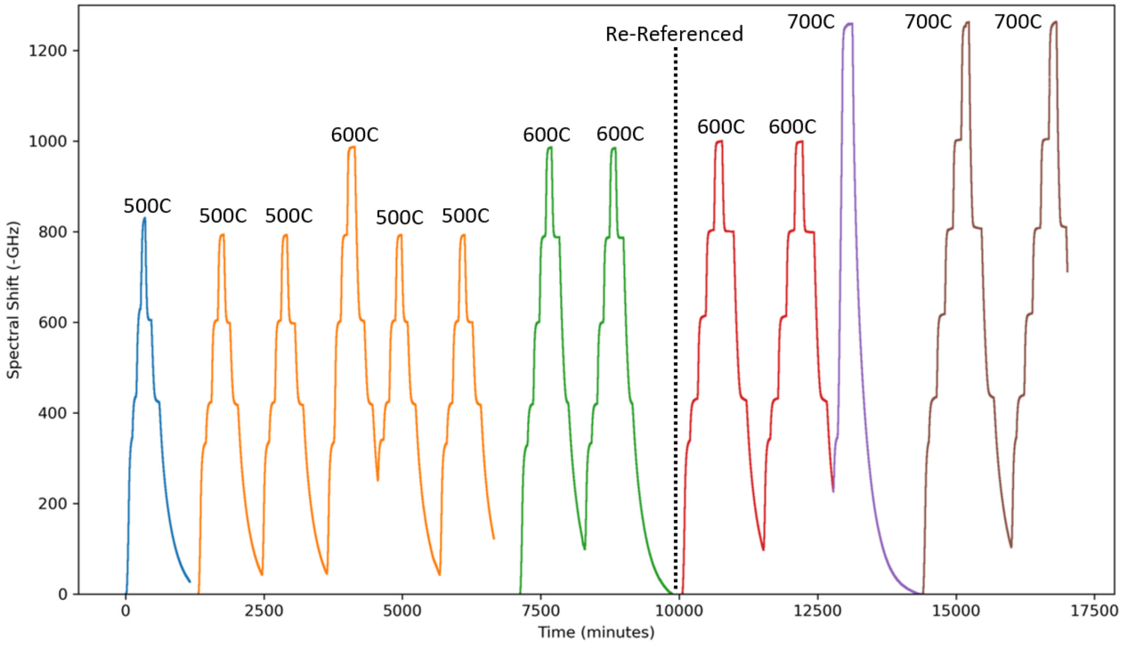

Figure 6. Spectral shift of Au-coated optical fiber over a full set of thermal cycles.

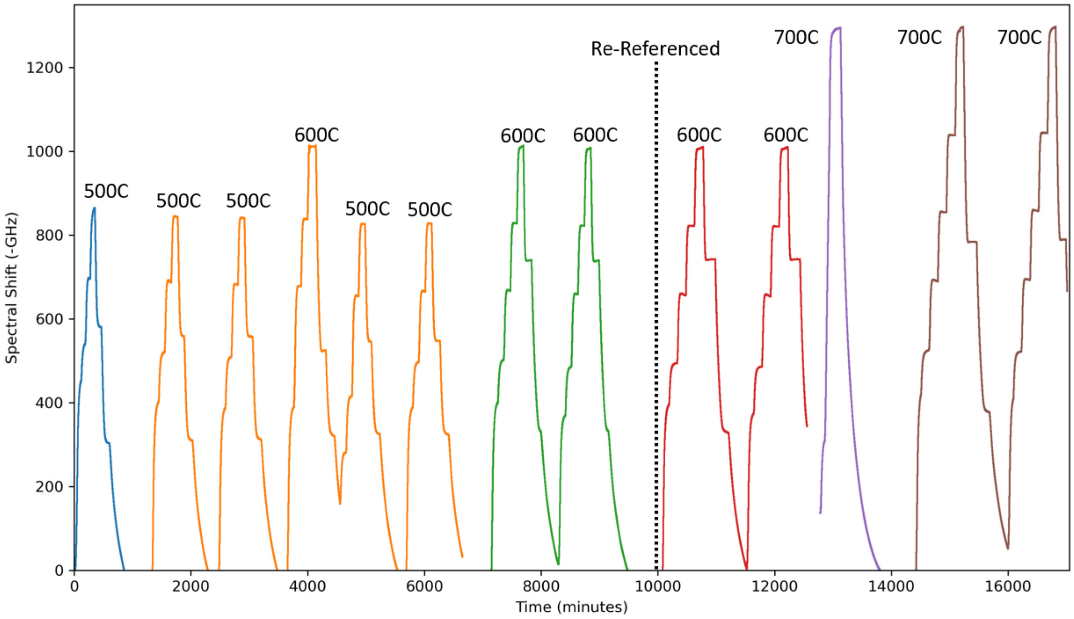

Figure 7. Spectral shift of Cu-C-coated optical fiber over a full set of thermal cycles.

Measurement repeatability is something crucial to sensor operation. Figure 8 shows the spectral shift response of the Au-coated fiber over the first three thermal cycles. The first heat was the very first time that the sensor had been thermally annealed. In the figure, the spectral shift at 500℃ for the initial heatup differed from cycles 2 and 3. This is not an issue if a thermal anneal is performed prior to running a calibration on a gold-coated sensor. The fiber's spectral shifts at 300°C and 400°C are identical for two thermal cycles during the ramp up and the cooldown. Figure 9 shows the Cu-C-coated optical fiber response for the same three cycles. As expected, the initial heatup shows a varied spectral shift from the thermal cycles. The Cu-C fiber's spectral shift is inconsistent at all temperature holds during heatup, being slightly smaller for cycle 3 than for cycle 2. Then, upon cooldown, the spectral shift at 300°C and 400°C significantly differs from the measured shift for both these cycles during heatup. The shift is inconsistent both within each individual cycle, and from one cycle to the next.

Figure 10 and Figure 11 show the fibers' response over thermal cycles 4, 5, and 6. These cycles entailed an initial heat to 600°C, followed by two repeated cycles at up to 500°C. The fibers were not re-referenced after the heat to 600°C. The Au-coated fiber responded consistently, with the spectral shift remaining unchanged at all temperatures. The response was consistent for both heating and cooling, even after the heat to 600°C. The response of the Cu-C fiber was, again, inconsistent. It was very inconsistent for cycles 5 and 6 when heating to 250°C and 300°C. For cycle 5 (i.e., the heat immediately following the heat to 600°C), the spectral shifts at 250°C and 300°C are significantly smaller (by approximately -100 GHz) than in cycles 2 and 3. The shifts in cycle 6 significantly differ from cycle 5 during heatup, but are closer to the initial shifts in cycles 2 and 3. The spectral shifts at 400°C and 300°C on the cooling side of the cycle differ from those on the heating side, as was the case in previous cycles. The shifts on the cooling side of cycles 5 and 6 are consistent from one cycle to the next, but not within each individual cycle. Note that 600°C is the recommended operating limit for the Cu-C-coated optical fiber.

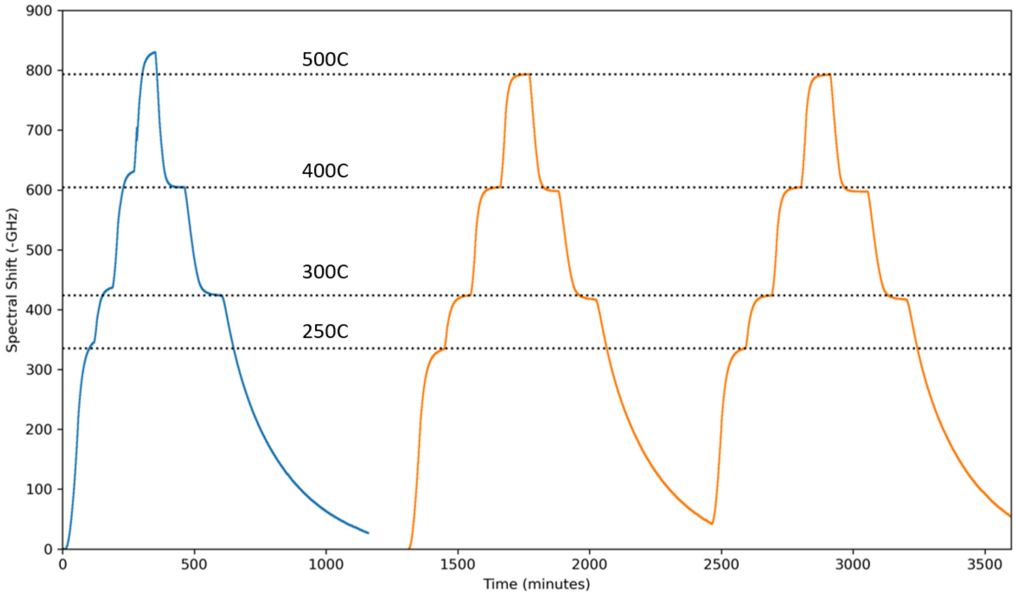

Figure 8. Spectral shift of Au-coated optical fiber during the first three thermal cycles, which consisted of a 500°C heat treat and two thermal cycles with a 500°C maximum temperature.

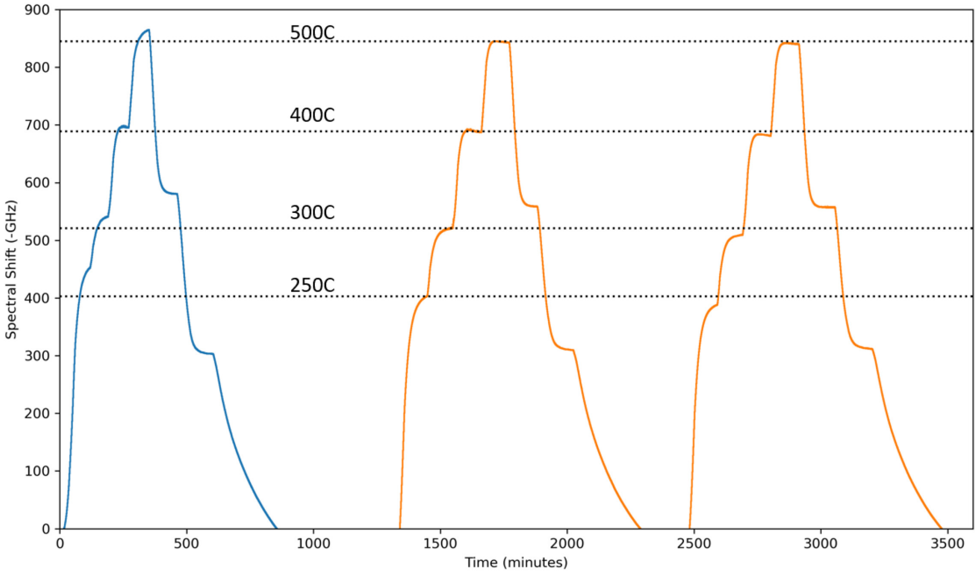

Figure 9. Spectral shift of Cu-C-coated optical fiber during the first three thermal cycles, which consisted of a 500°C heat treat and two thermal cycles with a 500°C maximum temperature.

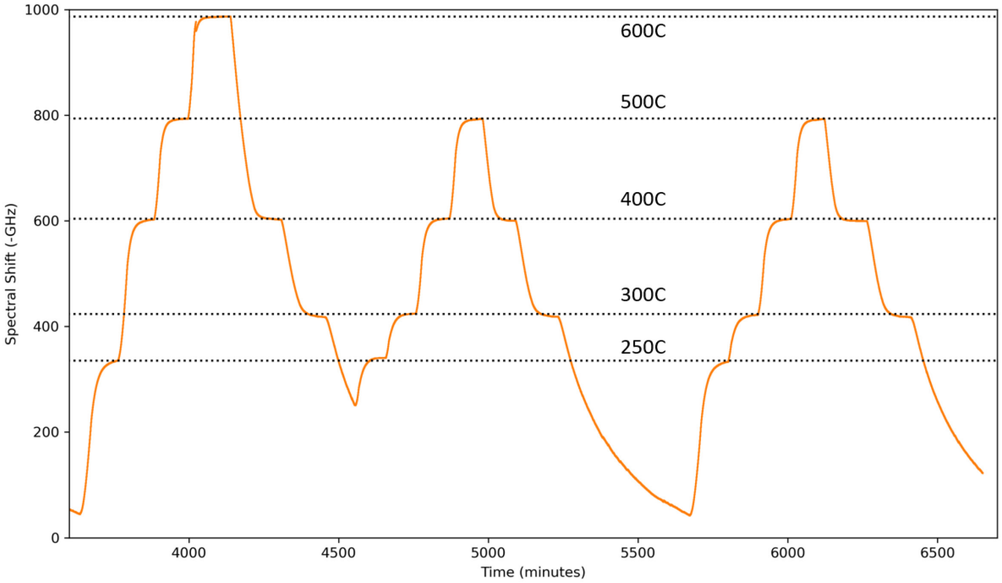

Figure 10. Spectral shift of Au-coated optical fiber during thermal cycles 4–6, which consisted of a 600°C heat treat and two thermal cycles with a 500°C maximum temperature.

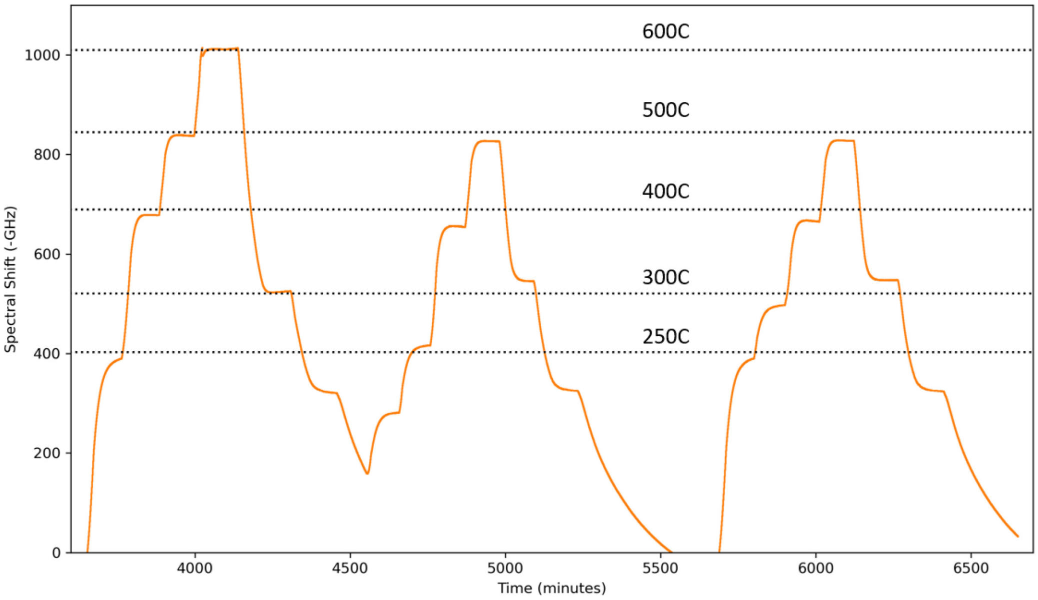

Figure 11. Spectral shift of Cu-C-coated optical fiber during thermal cycles 4–6, which consisted of a 600°C heat treat and two thermal cycles with a 500°C maximum temperature.

Figure 12 and Figure 13 show the Au-coated and Cu-C-coated fibers' response to thermal cycles 7 and 8. These two cycles are repeated cycles with peak temperatures of 600°C. The Au fiber again shows excellent repeatability in the spectral shift at all temperatures during both cycles, whether heating or cooling. On the other hand, the Cu-C fiber again showed unpredictable variability in the spectral shift while the fiber was heating, and an inaccurate but consistent shift between cycles for cooling. Cycles 9 and 10 are not shown because they represent the same temperature profiles as cycles 7 and 8, and were run immediately following sensor re-referencing. The fibers show the same response to cycles 9 and 10 as to 7 and 8. Figure 14 and Figure 15 show the fiber responses for cycles 11–13. This includes a thermal anneal to 700°C for the first time, and two cycles with a peak temperature of 700°C, which is the recommended peak operating temperature for the Au-coated optical fiber. Because the sensors were re-referenced between cycles 8 and 9, the spectral shifts at each temperature slightly differ from those in the previous cycles. The Au-coated optical fiber again reflected a consistent spectral shift at all temperatures. The full cooling tail of cycle 13 was not captured, due to a conflicting commitment regarding the ODiSI instrument. The Cu-C fiber was more consistent between cycles 12 and 13 than had previously been the case, but was still inaccurate within each individual cycle. Both fibers were intact, and the coating seemingly remained well-adhered to the fiber surface. No visible flaking or missing sections were observed on either fiber.

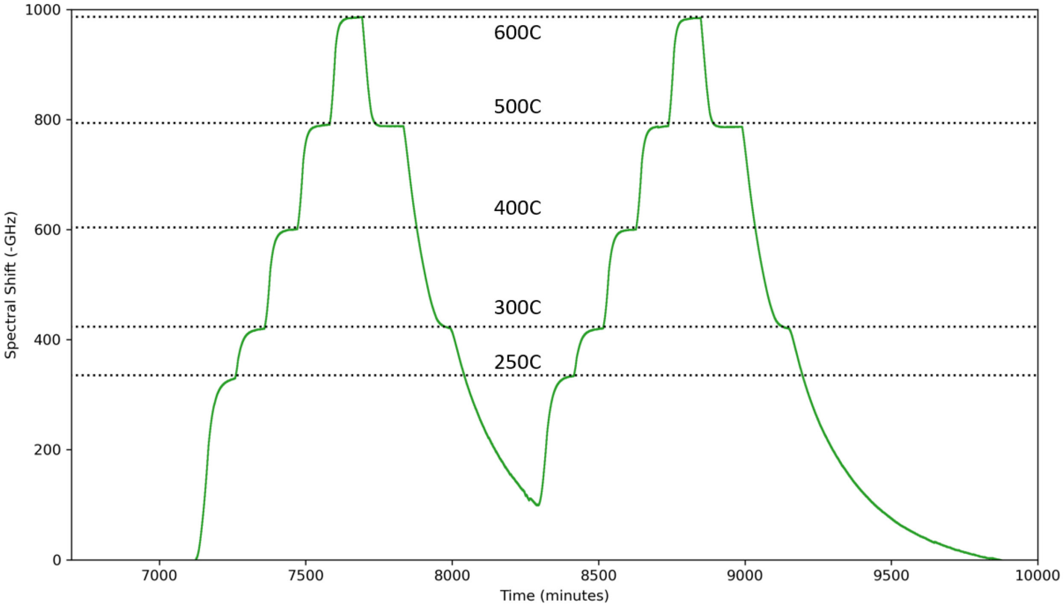

Figure 12. Spectral shift of Au-coated optical fiber during thermal cycles 7 and 8, which consisted of two thermal cycles with a 600°C maximum temperature.

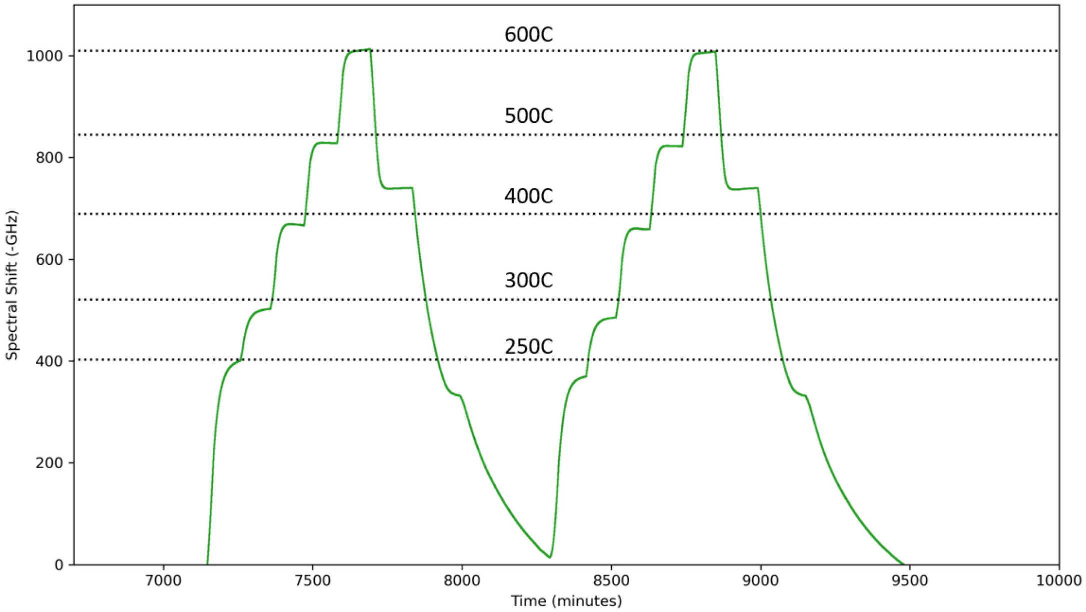

Figure 13. Spectral shift of Cu-C-coated optical fiber during thermal cycles 7 and 8, which consisted of two thermal cycles with a 600°C maximum temperature.

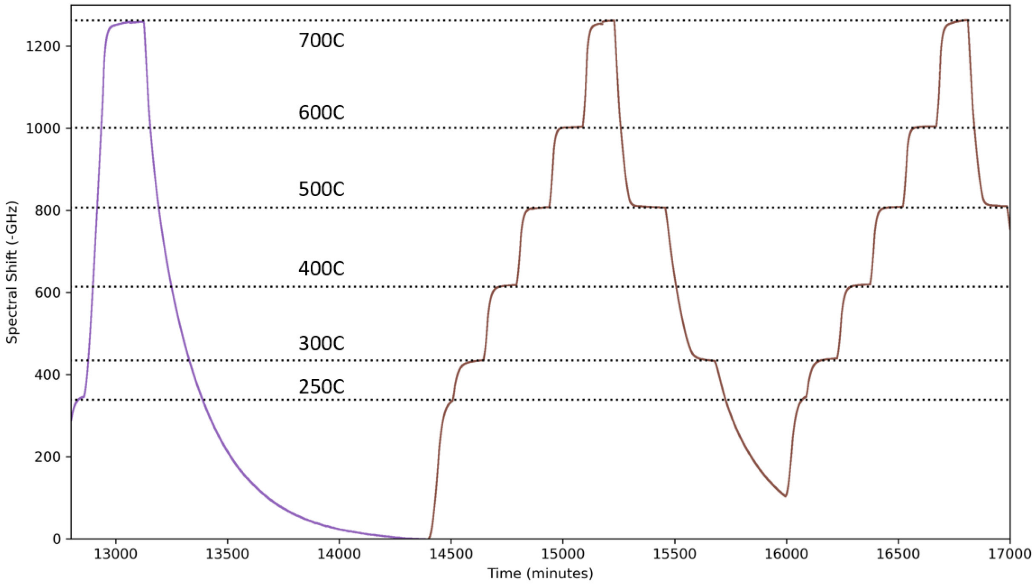

Figure 14. Spectral shift of Au-coated optical fiber during thermal cycles 11–13, which consisted of a 700°C heat treat and two thermal cycles with a 700°C maximum temperature.

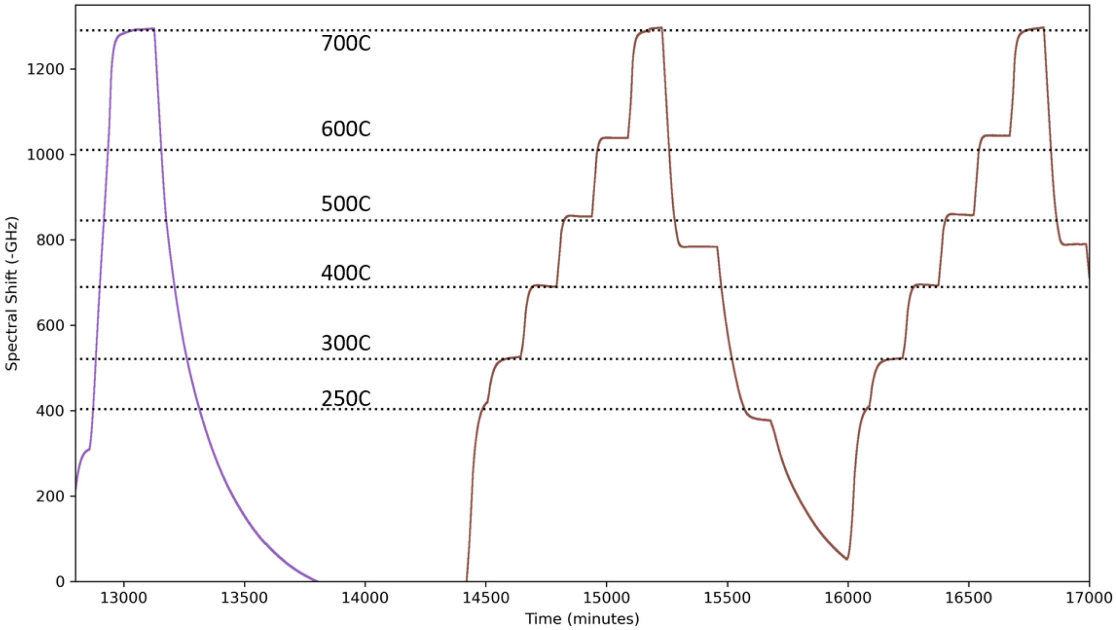

Figure 15. Spectral shift of Cu-C-coated optical fiber during thermal cycles 11–13, which consisted of a 700°C heat treat and two thermal cycles with a 700°C maximum temperature.

A consistent spectral shift response is crucial to sensors deployed in experiments. If the spectral shift is not repeatable at elevated temperatures, then the sensor cannot produce reliable information. The Cu-C-coated optical fiber was very inconsistent across all temperatures, even ones below the recommended operating limit. During the first thermal test, the inconsistency of the Cu-C-coated sensor was attributed to oxidation of the coating. However, even though the second thermal test was conducted in an argon environment to remove the potential for oxidation, the sensor continued to show unpredictable variation in its spectral shift measurements. This may be due to the copper layer slipping on the carbon layer, or perhaps the carbon delaminating from the silica glass. The Al-coated fiber performed well below aluminum's melting temperature of 600°C. The polyimide-coated fiber also provided a consistent response, but was mechanically fragile. The most mechanically robust and consistent response to temperature cycling was for the Au-coated optical fiber. For applications in which a fiber is adhered to a dominant bulk part (e.g., embedded in a metal structure), Cu-C-coated fiber may be a reasonable option. However, for optical frequency domain reflectometry, sensing via the Cu-C fiber is unsuitable. For applications below 600°C, an Al-coated optical fiber is a good economical choice. The aluminum coating may also be a preferred choice for applications in which a test must be handled post-irradiation. Activation of aluminum would be less of a concern, thanks to its shorter half-life, than would be the case for an Au-coated fiber. For applications intended for up to 700°C, Au-coated fiber is an excellent solution, as it provides a consistent spectral shift response to cyclical thermal testing. It also maintained the mechanical strength of the coating throughout the thermal testing. If a fiber sensor is to be deployed somewhere with little to no mechanical stresses or vibrations, an uncoated fiber or polyimide-coated fiber, which allows the coating to burn off, may represent an economical solution.

3. IN-CORE TESTING

Two main issues arise when deploying optical fibers in radiation environments: attenuation and signal drift. Pure silica core (PSC) optical fibers with a fluorine-doped (F-doped) cladding, as well as fibers with an F-doped core and clad optical fibers, have shown better resistance to radiation-induced attenuation than other traditional optical fiber technologies. Silica optical fibers have been thoroughly tested under various radiation environments. The highest total fast fluence a silica optical fiber has been tested to is 10^{21} n/cm^2. This testing was performed on PSC F-doped-clad single-mode silica optical fibers in the High Flux Isotope Reactor, revealing a blue shift in the fiber Bragg grating (FBG) wavelength that did not saturate, and corresponded to a 1000°C temperature drift in the measurement. [9] This shift could be detrimental to any sensing mechanism that is dependent on the refractive index change. Further investigation is needed to determine the mechanism behind this shift. The blue shift was not explained by radiation-induced compaction (RIC), and this work also showed that the PSC F-doped-clad optical fiber retained transmission post-irradiation. This significant result indicates that silica optical fibers can potentially be deployed for transmission at up to 10^{21} n/cm^2 fast fluence.

3.1 The Advanced Test Reactor Irradiation Methodology

Two PSC F-doped-clad optical fibers were deployed in an Advanced Test Reactor (ATR) experiment. They were contained in Inconel 600 capillary tubes inserted into the experiment capsule. Nine type-II FBGs were inscribed in each optical fiber by a company called FBGS. [10] The gratings were spaced 1 cm apart from each other; the outermost grating was 1 cm from the end of the fiber, and both ends of the fibers were cleaved to an 8-degree angle. Figure 16 shows the location of the fibers with respect to the ATR fuel. The two sensors were staggered to enable comparison between the end reflection and the amplitude of the gratings. This should help in differentiating between temperature and radiation-induced attenuation effects on the gratings. Prior to installation, the gratings were heat treated and calibrated. The heat treat profiles and calibration profiles are listed in Table 4. Figure 16 shows the spectra of the FBG sensors after the heat treat and calibration had been performed.

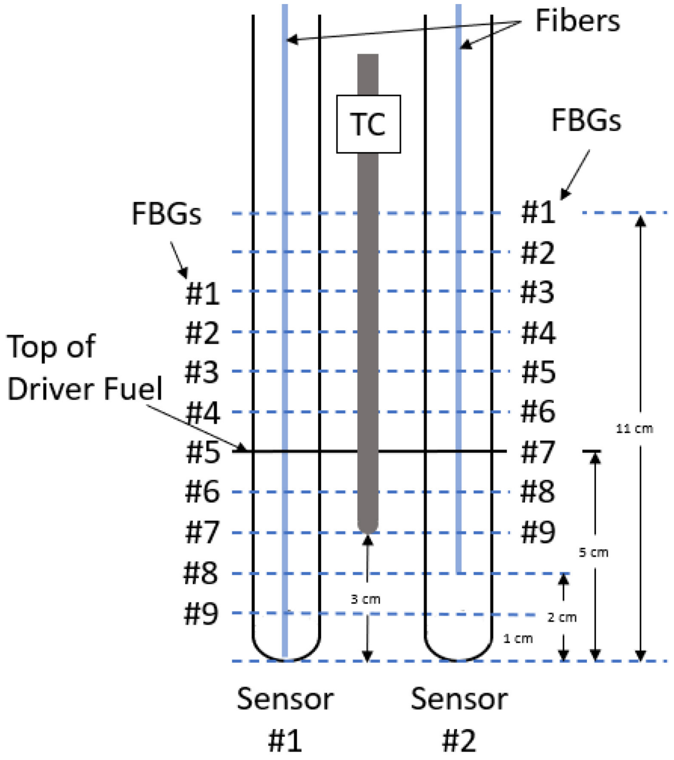

Figure 16. The two sensors were staggered in the metal capillary tubes.

Table 4. Heat treat and calibration temperatures for both FBG fiber optic sensors.

Sensor 1		Sensor 2	
	Heat Treat		
Temperature (°C)	Time (hours)	Temperature (°C)	Time (hours)
750	9	550	24
750	16	650	48
	Calibration		
100	4	100	4
200	4	200	4
300	4	300	4
400	4	400	5
500	4	500	5
600	4	600	5
250	3	250	3
700	5	650	5
		700	5

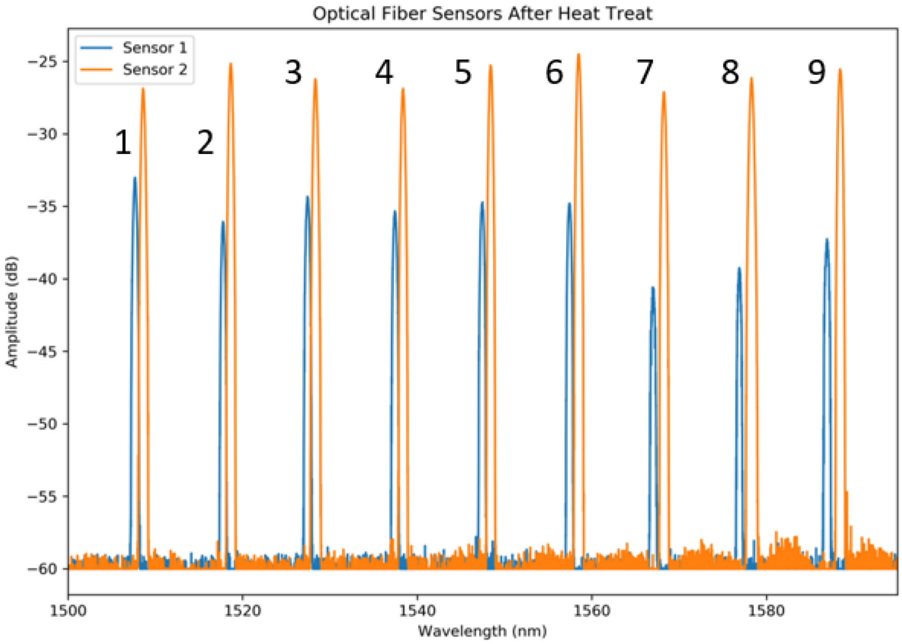

Figure 17. Spectra of both FBG sensors after heat treat and calibration at room temperature.

This experiment has remained installed for four ATR irradiation cycles, with one additional cycle remaining. The experiment contains dosimetry, but these data will be unavailable until post-irradiation examination of the experiment is complete. The total accumulated fluence experienced by the fibers was calculated by scaling the measured fluence rate of the west lobe by the ratio of the east and west lobe powers. This information is shown in Table 5 and Table 6.

Table 5. Fluence rates and accumulated fluence for each irradiation cycle at 1.83 cm elevation.

Cycle	Effective Full Power Days	Thermal Fluence Rate (n/cm^2/sec)	Fast (>1 MeV) Fluence Rate (n/cm^2/sec)	Total Accumulated Thermal Fluence during Cycle (n/cm^2)	Total Accumulated Fast (> 1 MeV) Fluence during Cycle (n/cm^2)	Total Accumulated Fluence during Cycle (n/cm^2)
168B	57.5	1.53E+13	2.22E+13	7.59E+19	1.10E+20	1.86E+20
169A	63.4	1.45E+13	1.86E+13	7.96E+19	1.02E+20	1.81E+20
171A	65.5	1.19E+13	2.53E+13	5.69E+19	1.21E+20	1.77E+20
171B*	65.5	1.19E+13	2.53E+13	6.76E+19	1.43E+20	2.11E+20
			Totals:	2.80E+20	4.76E+20	7.56E+20
* Estimated based on previous cycles and power histories						

Table 6. Total accumulated fluence at various elevations.

Location with Respect to the Sensor (cm)	Total Accumulated Thermal Fluence (n/cm^2)	Total Accumulated Fast (>1 MeV) Fluence (n/cm^2)	Total Accumulated Fluence (n/cm^2)
6.85	1.64E+20	2.18E+20	3.81E+20
1.83	2.80E+20	4.76E+20	7.56E+20
-3.26	8.32E+20	6.91E+20	1.52E+21

3.2 Results and Discussion

Several interesting phenomena occurred in the sensors over the course of the first two irradiation cycles. Both fiber optic sensors still provided a signal after a total accumulated fast fluence (>1 MeV) of approximately 2×10^{20} n/cm^2. Figure 18 shows the Bragg wavelength shifts for each of the nine FBGs in sensor 1 throughout the first two irradiation cycles. The wavelength shifts in Figure 18 reflect the change in wavelength from the post-anneal room-temperature peak wavelengths. The first 5.5 days of irradiation were missed due to an error in the data logging equipment. At the start of the data logging, FBGs 7, 8, and 9 in sensor 1 appeared to have already annealed out. The remaining FBGs experienced reduced amplitude. Significant thermal and flux gradients existed along the length of the sensors, due to their being placed at the top of the fueled region. A thermocouple collocated with the sensors measured a temperature range of 520°C–550°C over the first two irradiation cycles.

Over the course of the first irradiation cycle, all nine FBGs in sensor 1 annealed out and then regenerated and regained amplitude. The regained amplitude was still lessened in comparison to the initial amplitude, but remained stable over time. Figure 19 shows FBG 1 in sensor 1 at various times throughout the first two irradiation cycles. The grating loses amplitude until around 800 hours into the irradiation, experiences a period of no defined peak wavelength, then begins to regain amplitude at around 1200 hours. The reactor is in outage and the fiber is cooled to room temperature from around 1500 hours to approximately 4200 hours. The second irradiation cycle then begins, reheating the fiber. The FBG reaches a stable amplitude by around 4500 hours. The amplitude of FBG 1 at 4500 hours was reduced by approximately 9.5 dB in comparison to the reflected amplitude at time = 0.

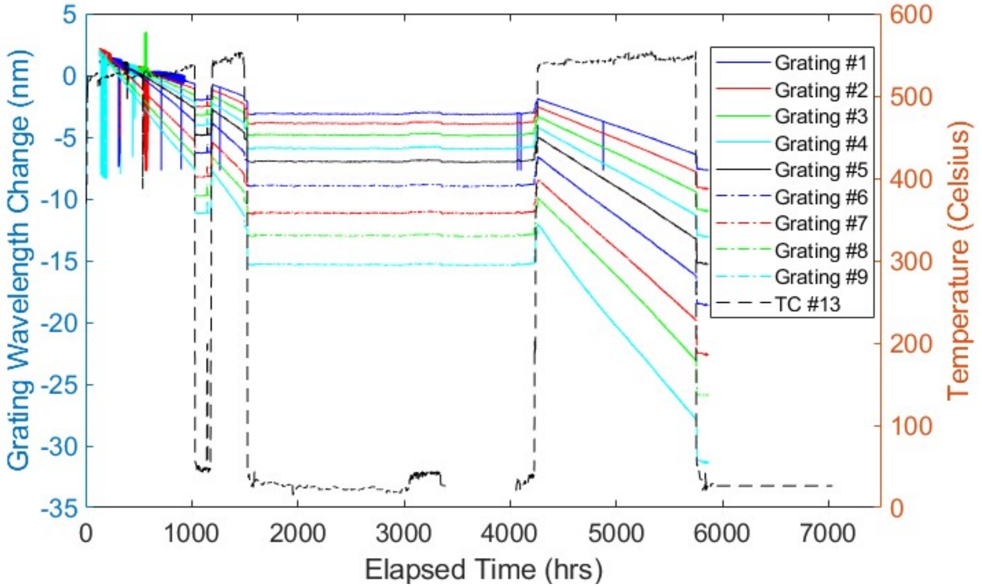

Figure 18. Wavelength shift in all nine FBGs in sensor 1 during the first two irradiation cycles.

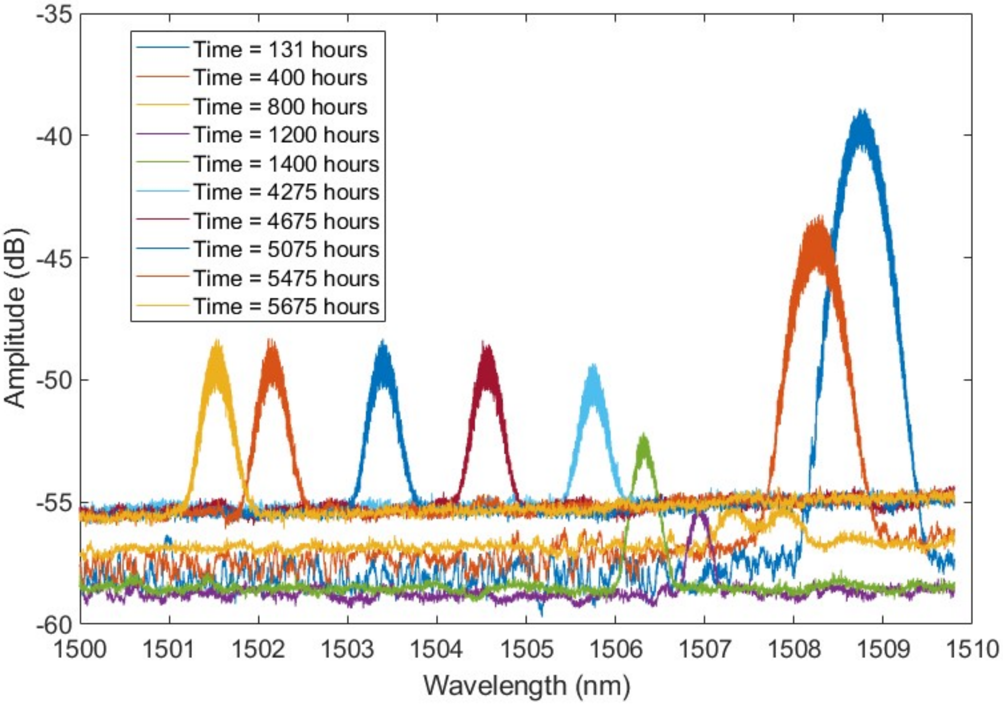

Figure 19. Sensor 1, FBG1, spectrum over time during irradiation cycles 1 and 2.

Figure 20 shows the Bragg wavelength shifts for the FBGs in sensor 2, that had a measurable center wavelength, for irradiation cycles 1 and 2. Not all the FBGs had a measurable peak wavelength, due to a significant variation in the baseline reflection. The full measured spectra of sensor 2 during irradiation cycles 1 and 2 are shown in Figure 21. Each displayed peak corresponds to an FBG. The baseline signal changes significantly during the irradiation. As shown in Figure 16, the physical end of sensor 2 is offset from the physical end of sensor 1 by 2 cm. The FBGs in sensor 2 underwent the same anneal and regeneration process applied to sensor 1, but in sensor 2 the process took longer both to anneal out and regenerate at elevated temperatures than it did in sensor 1. This is likely because the offset resulted in a shifted, lower-temperature environment for sensor 2.

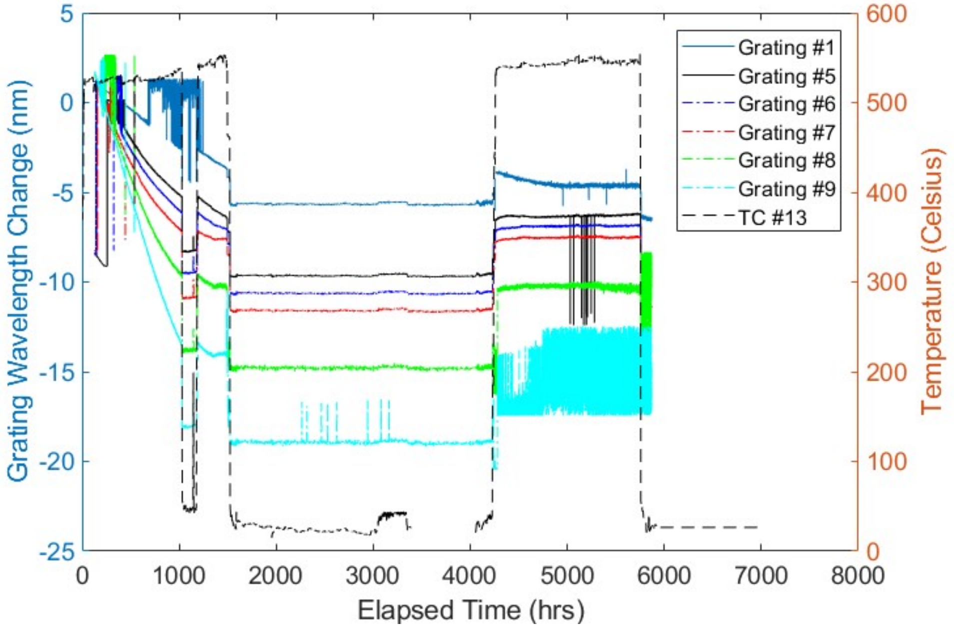

Figure 20. Wavelength shift of FBGs 1 and 5–9 in sensor 2 during the first two irradiation cycles.

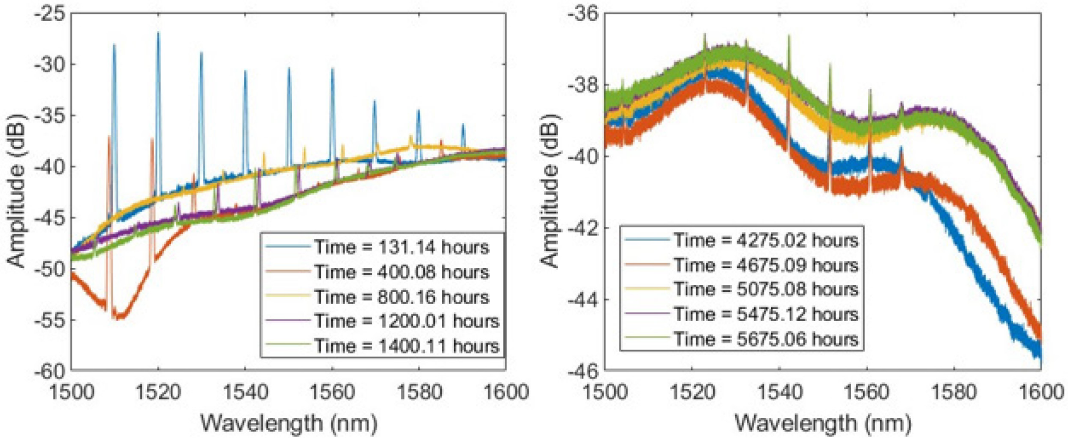

Figure 21. Sensor 2 spectrum during the first irradiation cycle (left) and the second irradiation cycle (right).

In addition to the regeneration that occurred during the first irradiation cycle, both fibers experienced a large amount of drift while under irradiation. A certain degree of shift to lower wavelengths is expected as a result of RIC. The measured peak wavelength for sensor 1, FBG 1, is shown in Figure 22. For sensor 1, FBG 9, it is shown in Figure 23. FBG 1 shifted around -3 nm linearly over the first irradiation cycle, and -4.5 nm over cycle 2, for a total shift of -7.5 nm. FBG 9 shifted -15.2 nm over cycle 1 and -16.1 over cycle 2, for a total shift of -31.3 nm. Figure 18 shows that all the FBGs in sensor 1 linearly shifted while under irradiation, with no indication of saturating. The FBGs all reflect different magnitudes of drift, due to the flux gradient along the length of the sensor.

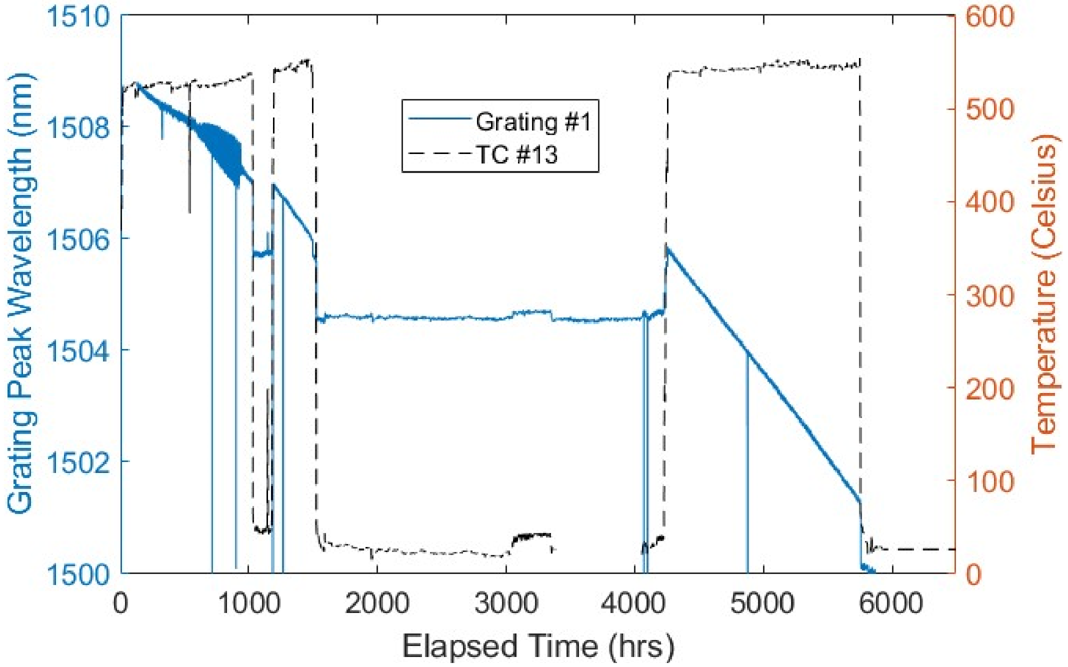

Figure 22. Sensor 1, FBG 1, peak wavelength shift during irradiation cycles 1 and 2.

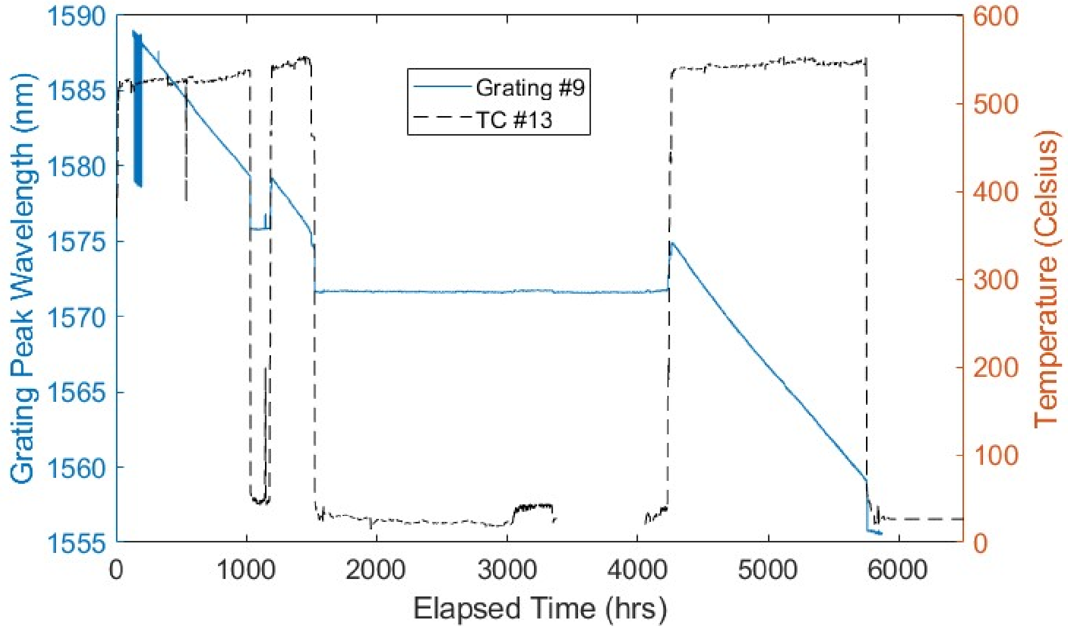

Figure 23. Sensor 1, FBG 9, peak wavelength shift during irradiation cycles 1 and 2.

Sensor 2 also experienced a blue shift in the FBG wavelengths. This shift was initially linear, but then saturated during cycle 2, as shown in Figure 24 for sensor 2, FBG 1. The same saturation effect was seen in all nine FBGs at different irradiation times and with various total shifts. FBG 9 was the first FBG to reach saturation. Its wavelength shift is shown in Figure 25. FBG 9 did not have a distinct peak wavelength in cycle 2, likely due to the aforementioned variation in baseline amplitude. FBG 7 had a distinct peak wavelength for the durations of both irradiation cycles, and saturated in cycle 1. This is seen in Figure 26.

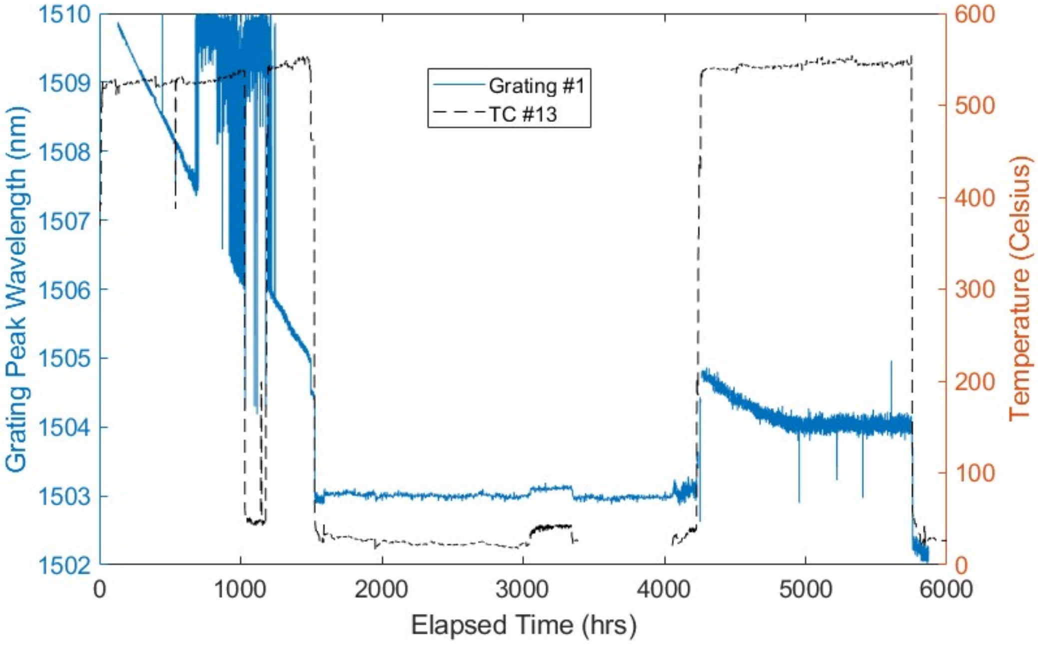

Figure 24. Sensor 2, FBG 1, peak wavelength shift during irradiation cycles 1 and 2.

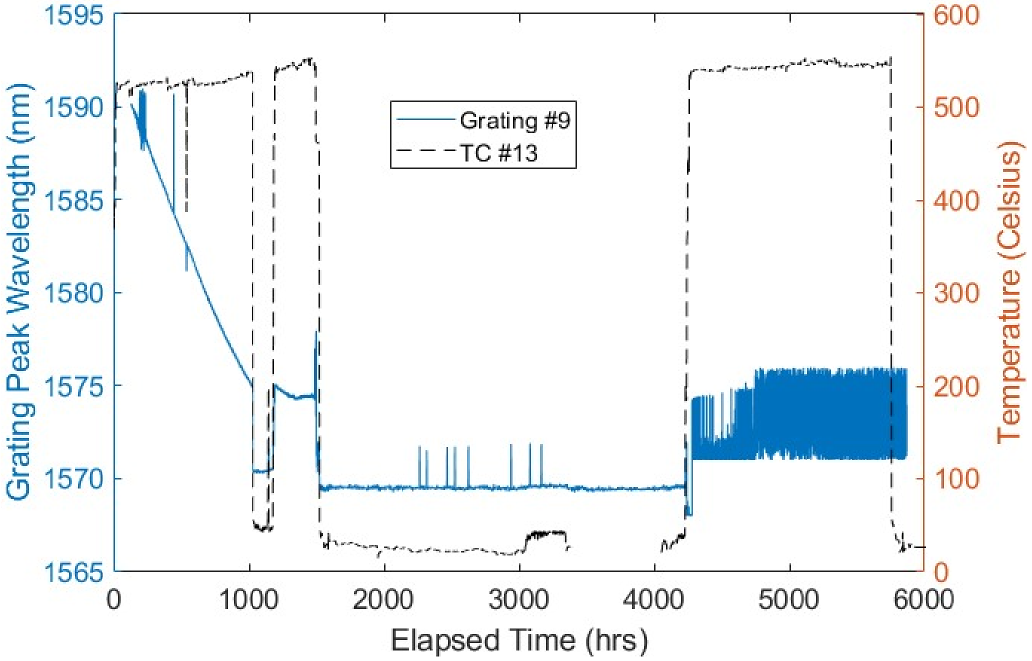

Figure 25. Sensor 2, FBG 9, peak wavelength shift during irradiation cycles 1 and 2.

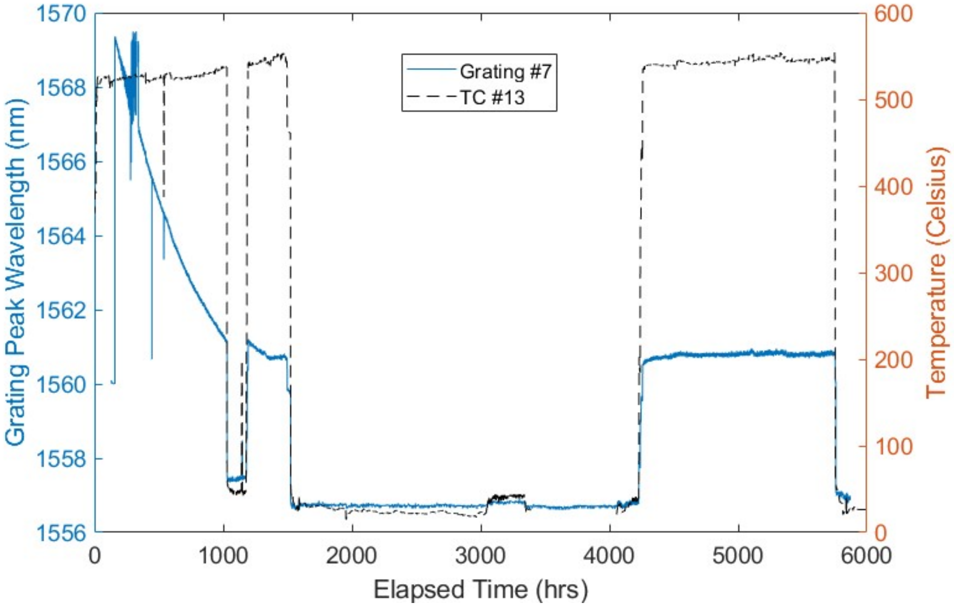

Figure 26. Sensor 2, FBG 7, peak wavelength shift during irradiation cycles 1 and 2.

Irradiation cycles 3 and 4 brought the total accumulated fast fluence to 4 × 10^{20} n/cm^2. Figure 27 shows the Bragg wavelength shift for sensor 1. FBG 1 had shifted so far that the grating wavelength was no longer in the range of the swept laser. FBGs 2–9 continued to undergo a linear negative wavelength shift while under irradiation throughout both cycles, with no indication of nearing saturation. FBG 2 had a total shift of -17.5 nm for all four cycles. FBG 9 had a total shift of approximately -54 nm. A standard FBG can have a temperature sensitivity of around 9-13 pm/°C. [11] The wavelength shift for sensor 1, FBG 9, corresponds to a temperature drift of approximately -5000°C.

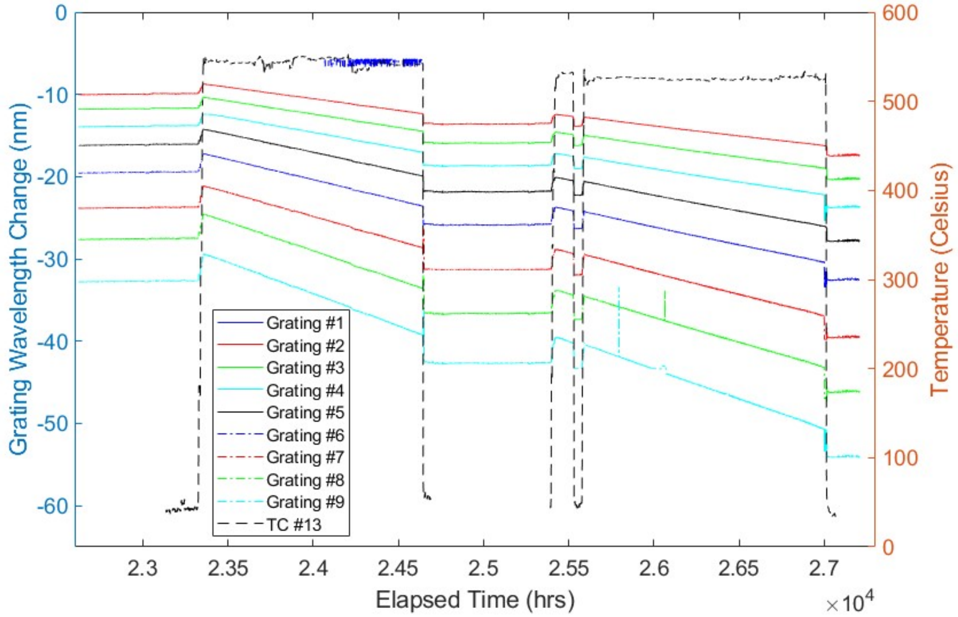

Figure 27. Wavelength shift in all nine FBGs in sensor 1 for irradiation cycles 3 and 4.

Figure 28 shows the wavelength shift in sensor 2. FBGs 1, 5, 6, 7, and 8 all possessed a measurable peak wavelength, and all five of those FBGs retained the saturation value and did not drift for the durations of both cycles 3 and 4.

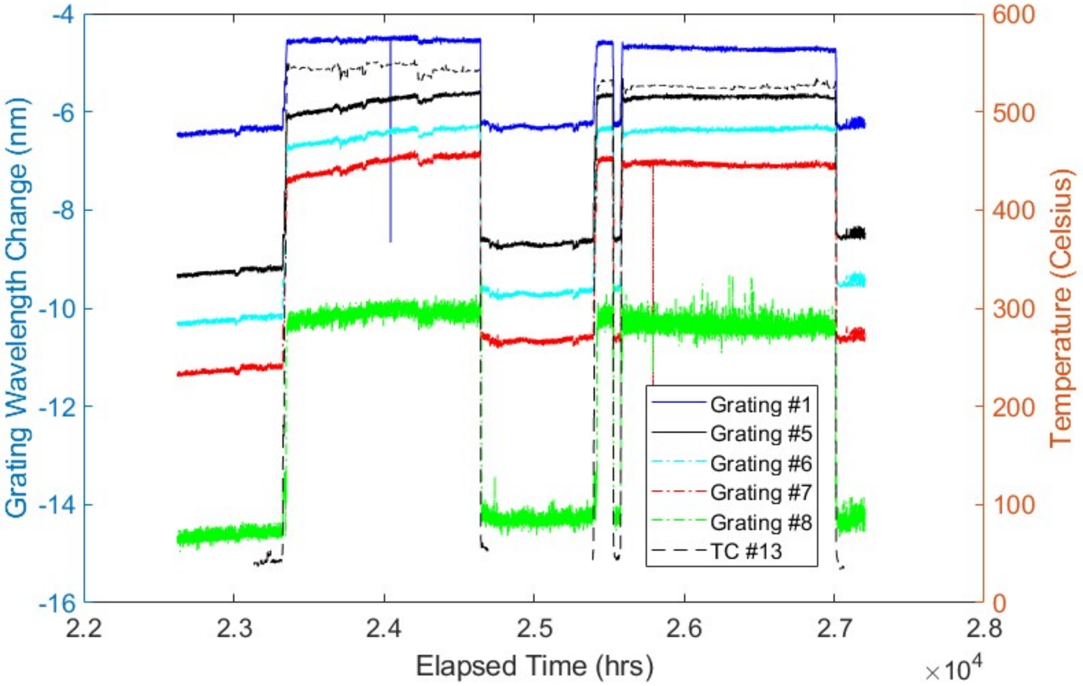

Figure 28. Wavelength shift of FBGs 1 and 5–8 in sensor 2 during irradiation cycles 3 and 4.

Regeneration of FBGs is a known phenomenon that has been utilized to create more thermally stable FBGs. The regeneration process involves thermally annealing a seed FBG until the amplitude is completely diminished, then a regenerated FBG returns with a slightly lower reflected amplitude. Regenerated FBGs have proven more thermally stable. [12] The reduction in amplitude of the gratings is much lower than for previous research conducted using standard Ge-doped optical fibers. Ge-doped optical fibers attenuate to a state in which there is complete light loss, making them unusable as sensors. The approximately 9.5 dB reduction in amplitude for sensor 1, FBG 9 (i.e., the FBG exposed to the highest fluence), can be tolerated by most sensing mechanisms. The continued transmission through both fibers is an encouraging result in regard to the use of silica optical fibers for extrinsic sensors such as pyrometers and Fabry-Perot cavities.

Intrinsic sensing applications would be unable to tolerate the drift in either sensor. Sensor 1 showed no indication of saturation, with the total drift being equivalent to approximately -5000°C. The drift in sensor 2, FBG 8, saturated at around -14.5 nm. This drift is still more than -1400°C, if the FBG is being used for temperature sensing. This value would only be allowable if a sensor was not needed for the initial irradiation and could be recalibrated at a known temperature after saturation was reached. This makes PSC F-doped-clad silica impractical for intrinsic measurements.

Some of the sensor drift is attributable to RIC. Previous studies on RIC showed that it would saturate in silica optical fiber at around 2%–3% volumetric change. [13-16] The linear compaction in the optical fiber causes a negative wavelength shift. However, the densification causes a positive index of refraction change that counteracts some of the negative wavelength shift stemming from RIC. Previous work found the shift in FBG wavelengths to be <-1 nm for a fast fluence of 10^{19} n/cm^2. Work by Zaghloul et al. [17] and Petrie et al. [9] both showed unsaturated blue shifts in PSC fiber at a fast fluence of up to 10^{20} and 10^{21} n/cm^2. Furthermore, the work by Petrie et al. showed the shift to be temperature dependent. In this work, both a thermal gradient and a flux gradient are seen along the length of the fiber. The rate of the drift is significant, indicating that the larger drift in FBG wavelengths may also be temperature dependent. Additional work with Ge-F-doped optical fibers saw a temperature-dependent saturation in wavelength shift at 10^{19} n/cm^2 fast fluence; this shift was a positive wavelength shift. [18] Sensors 1 and 2 were identical, apart from their anneal temperatures and the 2 cm offset. There was a degree of FBG overlap, so some locations in sensor 2 experienced the exact same conditions as in sensor 1. Sensor 1 was annealed at 750°C for 16 hours, and sensor 2 was annealed at 650°C for 48 hours.

High-fluence testing of silica optical fibers has presented a variety of different results, and further investigation is required to determine the mechanism behind the drift involved. The temperature dependence of the drift and the difference between regenerated FBGs and conventional FBGs indicate that it likely relates to the mechanism for grating regeneration.

4. CONCLUSIONS

Silica optical fibers have been investigated thoroughly for non-nuclear applications. In this work, silica optical fibers were tested under transient irradiation conditions as well as up to 4×10^{20} n/cm^2 fast fluence. The high-fluence testing of silica optical fiber resulted in one sensor drifting significantly, with no sign of saturation, while the other reached saturation after a single irradiation cycle in ATR. The research described herein facilitated and successfully deployed a distributed fiber optic sensor in a fueled experiment in order to meet the test's data objectives. Thermal testing of metal-coated silica optical fiber showed that a copper coating affects measurement repeatability. This is unacceptable for intrinsic measurements but may be allowable for extrinsic sensing. The gold-coated optical fiber performed well under thermal cycling at up to 700°C and provided repeatable temperature measurements. This work expanded the operational range of coated optical fibers from 400°C to 700°C.

Various results were achieved by using silica optical fiber at high fast fluence. Further work should be conducted to sufficiently characterize the mechanisms of drift in radiation-tolerant silica fiber at high fluence. This should include investigating how irradiation temperature, thermal annealing pre-treatments, and flux magnitude all affect the potential saturation of the drift.

5. REFERENCES

[1] Calderoni, P., et al. 2019. "Innovative sensing technologies for nuclear instrumentation." Idaho National Laboratory, INL/CON-18-52191-Revision-0. https://inldigitallibrary.inl.gov/sites/sti/sti/Sort_8942.pdf.

[2] Rempe, J., et al. 2011. "New In-Pile Instrumentation to Support Fuel Cycle Research and Development." Idaho National Laboratory, INL/EXT-10-19149. https://inldigitallibrary.inl.gov/sites/sti/sti/4781572.pdf.

[3] Wang, J., et al. 2010. "Distributed optical fiber temperature sensor applied in underground coal gasification system." *Asia Communications and Photonics Conference and Exhibition*, Shanghai, pp. 302—303. doi: 10.1109/ACP.2010.5682558.

[4] Naruse, H., et al. 2007. "Application of a distributed fibre optic strain sensing system to monitoring changes in the state of an underground mine." *Meas. Sci. Technol.*, **18**, 3202, doi:10.1088/0957-0233/18/10/S23. https://iopscience.iop.org/article/10.1088/0957-0233/18/10/S23/pdf.

[5] Lanticq, V., et al. 2009. "Soil-embedded optical fiber sensing cable interrogated by Brillouin optical time-domain reflectometry (B-OTDR) and optical frequency-domain reflectometry (OFDR) for embedded cavity detection and sinkhole warning system." *Meas. Sci. Technol.*, 20, p. 034018. https://iopscience.iop.org/article/10.1088/0957-0233/20/3/034018/pdf.

[6] IVG Fiber. n.d. "Metal-coated fiber." IVG Fiber. http://www.ivgfiber.com/metallized_fiber.htm.

[7] Wilson, B. A. and Blue, T. E. 2018. "Quasi-Distributed Temperature Sensing Using Type-II Fiber Bragg Gratings in Sapphire Optical Fiber to Temperatures up to 1300°C." *IEEE Sensors Journal*,

18: 20, pp. 8345—8351, doi: 10.1109/JSEN.2018.2865910. https://ieeexplore.ieee.org/document/8438888.

[8] Castrejón-Sánchez, V-H. et al. 2019. "Thermal Oxidation of Copper Over a Broad Temperature Range: Towards the Formation of Cupric Oxide (CuO)." *Materials Research Express,* **6**, 075909. https://iopscience.iop.org/article/10.1088/2053-1591/ab1662/pdf.

[9] Petrie, C. M. and Sweeney, D. C. 2023. "Enhanced backscatter and unsaturated blue wavelength shifts in F-doped fused silica optical fibers exposed to extreme neutron radiation damage." *Journal of Non-Crystalline Solids*, **615**, 122441, ISSN 0022-3093, https://doi.org/10.1016/j.jnoncrysol.2023.122441.

[10] FBGS. n.d. "Tailored fiber optic sensing components & solutions." FBGS. https://fbgs.com/.

[11] Ghosh, B. and Mandal, S. 2023. "Fiber Bragg grating-based optical filters for high-resolution sensing: A comprehensive analysis." Results in Optics, **12**, 100441, ISSN 2666-9501, https://doi.org/10.1016/j.rio.2023.100441.

[12] Polz, L., et al. 2021. "Regenerated Fibre Bragg Gratings: A critical assessment of more than 20 years of investigations." *Optics & Laser Technology*, **134**, 106650, ISSN 0030-3992, https://doi.org/10.1016/j.optlastec.2020.106650.

[13] Girard, S., et al. 2013. "Radiation Effects on Silica-Based Optical Fibers: Recent Advances and Future Challenges." *IEEE Transactions on Nuclear Science*, **60**: 3, pp. 2015—2036, doi: 10.1109/TNS.2012.2235464. https://ieeexplore.ieee.org/document/6457426.

[14] Primak, W. 1958. "Fast-neutron-induced changes in quartz and vitreous silica." *Phys. Rev. B*, **110**, no. 6, pp. 1240–1254.

[15] Petrie, C. M., Birri, A., and. Blue, T. E. 2019. "High-dose temperature-dependent neutron irradiation effects on the optical transmission and dimensional stability of amorphous fused silica." *Journal of Non-Crystalline Solids*, **525**, 119668, ISSN 0022-3093, https://doi.org/10.1016/j.jnoncrysol.2019.119668.

[16] Wootton, A., Thomas, B., and Harrowell, P. 2001. "Radiation-induced densification in amorphous silica: A computer simulation study." *J. Chem. Phys.* **115**:7 3336–3341. https://doi.org/10.1063/1.1387039.

[17] Zaghloul, M. A. S., et al. 2018. "Radiation resistant fiber Bragg grating in random air-line fibers for sensing applications in nuclear reactor cores." *Opt. Express*, **26**:9, 11775—11786. https://opg.optica.org/oe/fulltext.cfm?uri=oe-26-9-11775&id=385858.

[18] Fernandez, F., et al. 2006. "Chemical composition fiber gratings in a high mixed gamma neutron radiation field." *IEEE Transactions on Nuclear Science*, **53**:3, pp. 1607—1613, doi: 10.1109/TNS.2005.863273. https://ieeexplore.ieee.org/document/1645077.